Journal of Alloys and Compounds 895 (2021) 162592

Contents lists available at ScienceDirect

Journal of Alloys and Compounds

journal homepage: www.elsevier.com/locate/jalcom

Thermochemical heat storage performances of magnesium sulphate confined in polymer-derived SiOC aerogels

Andrea Zambotti[a,*], Francesco Valentini[a], Emanuele Lodi[a], Alessandro Pegoretti[a], Václav Tyrpekl[b], Soňa Kohúteková[b], Gian Domenico Sorarù[a], Matouš Kloda[d], Mattia Biesuz[a,b,c]

[a] Department of Industrial Engineering, University of Trento, Via Sommarive 9, 38123 Trento, Italy
[b] Department of Inorganic Chemistry, Faculty of Science, Charles University, Hlavova 8, 2030 Prague, Czech Republic
[c] Institute of Plasma Physics of the Czech Academy of Sciences, Za Slovankou 3, 182 00 Prague, Czech Republic
[d] Institute of Inorganic Chemistry, The Czech Academy of Sciences, Husinec-Řež 250 68, Czech Republic

ARTICLE INFO

Article history:
Received 16 September 2021
Received in revised form 27 October 2021
Accepted 1 November 2021
Available online 6 November 2021

Keywords:
Ceramic
Chemical synthesis
Thermochemistry
Kinetics

ABSTRACT

The thermochemical heat storage performances of hygroscopic magnesium sulphate ($MgSO_4$) can be improved by dispersing it within a porous matrix. However, the host material must be able to bear the intense stresses developed by the hydration of the salt. In this work, we report the first use of a polymer-derived SiOC ceramic aerogel as host for the confinement of $MgSO_4$ for seasonal thermal energy storage, providing a way to easily tune its final porosity to achieve controllable mass fractions of salt in the so-obtained composite. Besides, the distinctive mesoporosity of ceramic aerogels guarantee a free path for water vapour to rapidly hydrate $MgSO_4$ while avoiding the breakage of the composite. Vacuum impregnation of the aerogel samples led to a composite with a maximum of 59.1%*wt* of $MgSO_4$.1 H_2O and a complete hydration in 60 min under H_2O saturated air.

1. Introduction

According to the European Environment Agency (EEA), the greenhouse gases emissions related to electricity generation from stationary power plants decreased by 9.1% between 2018 and 2019 as a consequence of a partial replacement of coal with natural gas [1]. However, faster decarbonization and a consequent transition towards renewable energy sources are required to mitigate climate change and meet the environmental targets planned by the European Union [2]. Nevertheless, the power that can be generated from natural sources, such as sunlight, usually suffers from fluctuations related to the direct availability of the source itself. Therefore, it is fundamental to store the energy that is produced in excess to provide it when the energy demand cannot be satisfied through a direct conversion from the natural source. In this scenario, thermal energy storage (TES) is one of the most promising solutions.

TES technologies are based on the storage of heat within a material in the form of sensible heat, latent heat, or thermochemical heat, exploiting heat capacity, phase change enthalpy, or chemical reactions, respectively. Among the strategies developed during the last decades, thermochemical energy storage is the most energy-dense and efficient one, as it provides long-term heat storage under the form of chemical potential energy, with zero heat losses and a virtually infinite storage time [3]. This peculiarity of long-term TES is extremely appealing as it has the potential to provide a heat supply during the coldest periods of the year. Moreover, the specific hydration enthalpies (up to ≈ 10^3 J g^{-1}) in many cases can exceed the typical latent heat of fusion exploited in latent heat TES devices (≈ 10^2 J g^{-1} for low temperature, ≈ 250–500 J g^{-1} for medium-high temperature TES) [4,5]. Thus, thermochemical heat storage (TCHS) appears a rather promising tool to store huge amounts of energy in a limited mass [6]. This is a fundamental requirement for the development of grid-scale TES devices which would allow a real and substantial shift toward renewable energy sources.

Within the thermochemical heat storage class, sorption TES (STES) is based on sorption/desorption reactions, such as hydration/dehydration mechanisms, requiring an absorbent and a vapor phase, so that its TES efficiency is strictly dependent on reactions rates, reactors design and on the selected materials [7]. In recent years, STES systems involving the use of water vapor and salt hydrates as sorbent materials have been deeply studied for household and solar

* Correspondence to: University of Trento, Via Sommarive 9, 38123 Trento, Italy.
E-mail address: andrea.zambotti-1@unitn.it (A. Zambotti).

https://doi.org/10.1016/j.jallcom.2021.162592
0925-8388/

energy harvesting applications. As a matter of fact, a great variety of different salt hydrates are available for these purposes, and great effort has been made to define the most promising ones from a theoretical point of view [8].

However, the efficiency of systems using neat salt hydrates is remarkably lower than the theoretical one. The reasons are several and of fundamental importance. Firstly, as absorption proceeds, the volumetric expansion of the hydrating salt determines the closure of a pathway for vapor, thus inhibiting the hydration process. Secondly, the low thermal conductivity of salt hydrates, usually smaller than 1 $W\cdot(m\cdot K)^{-1}$, hinders heat extraction from a STES reactor [9]. Finally, salts hydrates are mechanically unstable and prone to sintering, so they must be confined and stabilized within a porous support material able to avoid the salts particle consolidation and coalescence [10].

Among the different salt hydrates, $MgSO_4$ is among the most promising ones thanks to its high thermochemical energy density (1265 $J\cdot g^{-1}$), the thermochemistry in the working temperature range of solar collectors, its low cost, its abundance, and because it is harmless [11]. The use of many different porous supports for this salt can be found in scientific literature, for example, zeolites [11–15], attapulgite and vermiculite [16,17], porous glasses and silica gels [18,19], expanded graphite, activated carbon [20], silicone foams [21], and metals [22]. However, while metal alloys mainly suffer from electrochemical corrosion phenonema due to the contact with hydrated salts, ceramic supports are characterized by rather low thermal conductivity [23,24]. Moreover, ceramics are usually not electrically conductive, thus this type of scaffold cannot be used to convert and store (in the form of heat) the excess of electrical energy produced for instance by wind, hydroelectric or photovoltaic energy plants. Carbon-based supports, on the other hand, are rather fragile and flammable. In this scenario, the polymer-derived ceramic (PDC) route represents an advantageous path to synthesize porous ceramics with specific properties such as mechanical stability, electrical conductivity and, chemical inertness. As a matter of fact, the PDC route allows to produce complex ceramic systems such as SiCN, SiOC and SiBCN through the pyrolysis in a controlled atmosphere of a preceramic polymer. As such, the elemental and phase composition of the final product can be easily controlled by adjusting the chemistry of the preceramic compound [25].

For the first time, in the present work we report on the use of a polymer-derived SiOC aerogel as support material for the stabilization of $MgSO_4$. The rationale behind this choice relies on the peculiar structure of the SiOC aerogel consisting in a strong silicon oxycarbide network (providing mechanical stability) [26], and a free carbon phase displaying electrical conductivity [27]. In fact, the ability of the ceramic scaffold to conduct electricity could provide an efficient root to convert and store the excess of electric energy.

2. Experimental procedure

2.1. Synthesis of the aerogels

Preceramic polymer SPR-036 was purchased from Starfire Systems Inc (NY, USA). It is a transparent liquid with a viscosity of 50 – 500 cp and serve as precursor for the SiOC system.

For the synthesis, n-hexane (Panreac, CAS: 110–54–3) was selected as solvent for the gelification and divinylbenzene (DVB, Sigma Aldrich, CAS: 1321–74–0) as crosslinking agent. Karstedt's catalyst (Sigma-Aldrich, Saint Louis, MO, USA, CAS: 68478–92–2) containing 2% platinum in xylene was diluted to 0.1% Pt in the same solvent before use. The recipe was tuned to have a 1:1 wt ratio between SPR-036 and DVB and adding 50 µl of diluted catalyst per gram of polymer while the solvent volume content was set to 80% and 90%. Varying the solvent fraction is a method for tuning the total volume of pores in the final product [28]. The rationale behind the use of a high amount of DVB resides in the necessity of having highly crosslinked gels able to sustain shrinkages during the ceramic conversion [29].

Table 1
Labeling of SPR-036 based aerogels reported in this work.

Precursor	Solvent (vol%)	Crosslinking T (°C) / t (h)	Pyrolysis T (°C)	Neat aerogels	Impregnated aerogels
SPR-036	80	200 / 24	–	S8	–
			800	S8_p8	iS8_p8
			1000	S8_p10	iS8_p10
	90	200 / 24	–	S9	–
			800	S9_p8	iS9_p8
			1000	S9_p10	iS9_p10

In a typical synthesis, the reagents were mixed in a Parr digestion vessel (Model 4749 Parr, Moline, IL, USA), which was further placed in an oven kept at defined conditions to promote the gel formation. In particular, SPR-036 based gels were crosslinked at 200 °C for 24 h.

The so-obtained gels were then subjected to a multi-step solvent exchange with fresh n-hexane, and then loaded into a customized supercritical reactor filled with liquid CO_2. After 3 days and 6 solvent exchanges (occurring at 10 °C and 40 bar), the fresh solvent was completely substituted with liquid carbon dioxide. Supercritical drying followed. Dried aerogels were finally subjected to the ceramization process through pyrolysis in nitrogen at 800 °C or 1000 °C. After obtaining the ceramic aerogels, they were vacuum-impregnated in saturated magnesium sulfate (Honeywell, CAS: 7487–88–9) water solution and subsequently dried to remove water. Table 1 reports the adopted labeling for the sample set.

2.2. Characterization methodology

Nitrogen physisorption was performed at 77.3 K with a BK300C (3P Instruments GmbH, Germany) to assess the aerogels specific surface area (SSA) and the pores size distribution. A preliminary degassing was performed holding the specimens at 200 °C for 2 h. Hg porosimetry was carried out in parallel to nitrogen physisorption to cover a wider pore size range from 100 µm down to 10 nm. A Porosimeter 2000 (Carlo Erba, Milano, Italy) was used for such a purpose, setting a pressure range of 0.2–2000 bar at 20 °C. Helium picnometry was performed with a AccuPyc 1330 pycnometer (Micromeritics, Norcross, GA, USA) to assess the skeletal density of neat aerogels.

Thermogravimetric and differential thermal analysis (TG/DTA) was performed on the composite specimens using a Mettler TG50 MT5 (Mettler-Toledo, CH) in air flow using a bubbler to introduce moisture into the gas, supposing 100% RH at ambient pressure. A Netzsch STA 409 thermobalance was used to define the thermal stability of the aerogels in oxidative environment of pure air (100 cc min^{-1}). In this latter case, the heating rate was set to 20 °C min^{-1} to reach 1200 °C.

The morphologies of the bare aerogels and derived composites were observed with a Gemini SUPRA 40 Scanning Electron Microscope (Carl Zeiss, Germany) equipped with a field emission gun. X-ray diffraction (XRD) patterns of non-impregnated and impregnated specimens were acquired with a a PANalytical X'Pert PRO diffractometer equipped with a Cu Kα source, secondary monochromator, and a PIXcel position-sensitive detector.

The characterization of the chemical bonds present in preceramic aerogels, as well as in ceramic and impregnated aerogels was carried out with a Thermo Nicolet 6700 FTIR spectrometer equipped with a SpectraTech Inspect IR Plus accessory in ATR mode (Si crystal) in the 650–4000 cm^{-1} region with 4 cm^{-1} resolution (Happ-Genzel apodization, MCT-A detector).

The Raman spectra were recorded on a Thermo Scientific DXR Raman Microscope interfaced to an Olympus microscope

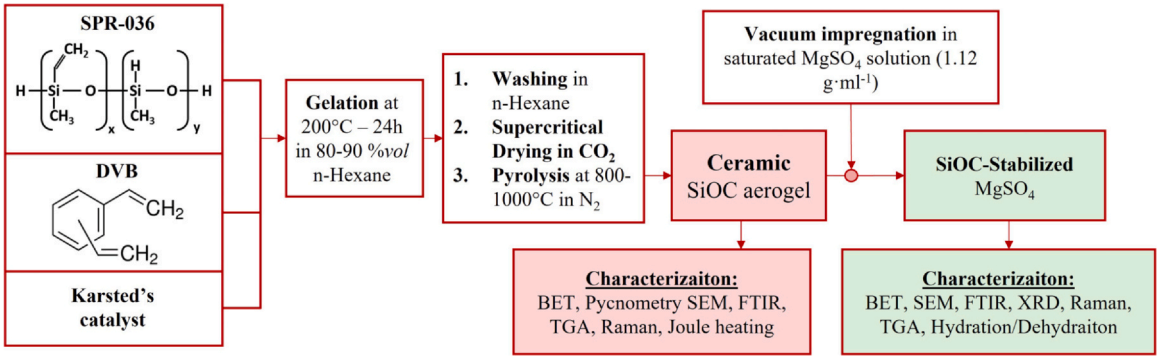

Fig. 1. Flowchart of the synthesis and characterization of the samples reported in the present work.

(objective 10x) in the 50 – 3300 cm^{-1} spectral region with approx. 5 cm^{-1} resolution to gather information on the distribution of carbon within the ceramic specimens. The power of frequency-stabilised single mode diode laser (780 nm) impinging on the sample was 2 mW.

To assess the possible use of these composites for electrical to thermal energy conversion, a FLIR E60 (emissivity = 0.86) thermocamera was employed to visualize and acquire the thermal response of a specimen under a variable applied voltage as a function of time.

Finally, Fig. 1 briefly summarizes the specimens synthesis and the further characterization procedure.

3. Results and discussion

3.1. Characterization of ceramic aerogels

Fig. 2 shows the N_2 adsorption/desorption isotherms of the ceramic aerogels together with the Barrett-Joyner-Halenda (BJH) incremental pore volume distribution. According to the IUPAC classification, all the curves present the typical shape of a Type IV isotherm, which is relative to mesoporous sorbents, with H2 hysteresis loop determined by capillary condensation at high P/P_0 [30]. The specific surface area of the aerogels is in the range 170 – 250 $m^2\ g^{-1}$ and decreases as the pyrolysis temperature increases from 800 °C to 1000 °C (Table 2). This phenomenon is related to a partial closure of pores smaller than 100 nm as evicendenced by the decrease of the BJH total pore volume (insets in Fig. 2 and Table 2). The SSA does not vary much when comparing aerogels obtained using different amounts of solvent (see for instance S8 and S9 samples in Table 2).

On the other hand, the solvent fraction has a relevant impact on the results of Hg porosimetry. As a matter of fact, S9_p8 and S9_p10 specimens are characterized by a porosity of 79.2% and 80.5%, respectively, while S8_p8 and S8_p10 both reach 58.8%. Macropores (wider than 50 nm), which are hardly detectable with N_2 physisorption are responsible for these results; infact, the BJH total pore volume measured by N_2 physisorption is substantially independent on the solvent load (Table 2).

Table 2
Nitrogen physisorption, Hg porosimetry and He pycnometry results on neat aerogels.

	S8_p8	S8_p10	S9_p8	S9_p10
BET SSA ($m^2\ g^{-1}$)	253.4	171.4	247.6	202.0
BJH V_{tot} pore ($cm^3\ g^{-1}$)	0.59	0.43	0.59	0.43
Skeletal density (g cm^{-3})[a]	1.74	1.83	1.77	1.89
Porosity (%)	58.8	58.8	79.2	80.5
Total volume of pores ($cm^3\ g^{-1}$)[b]	0.82	0.78	2.15	2.18

[a] He picnometry.
[b] Hg porosimetry.

Finally, pyrolysis temperature defines the skeletal density of the final product, which increases from 1.74 to 1.77 g cm^{-3} at 800 °C to 1.83–1.89 g cm^{-3} at 1000 °C regardless of the preceramic composition (Table 1).

Thermogravimetric analyses were performed in air flow to define the thermal stability of the obtained SiOC aerogels. From Fig. 3 it can be stated that no differences can be observed in terms of onset of thermal degradation between the two kinds of aerogel. At 250 °C all compositions undergo a preliminary oxidation of residual Si-CHx-Si bonds of the ceramic network, associated to a weight gain of 10% due to the insertion of bivalent oxygen atoms. After that, free carbon starts to oxidize from 450° to 500°C, leading to a weight loss of 25–27%*wt* for S8 and S9, respectively. In any case, all aerogels can be exposed to 250 °C without any damage of the ceramic network.

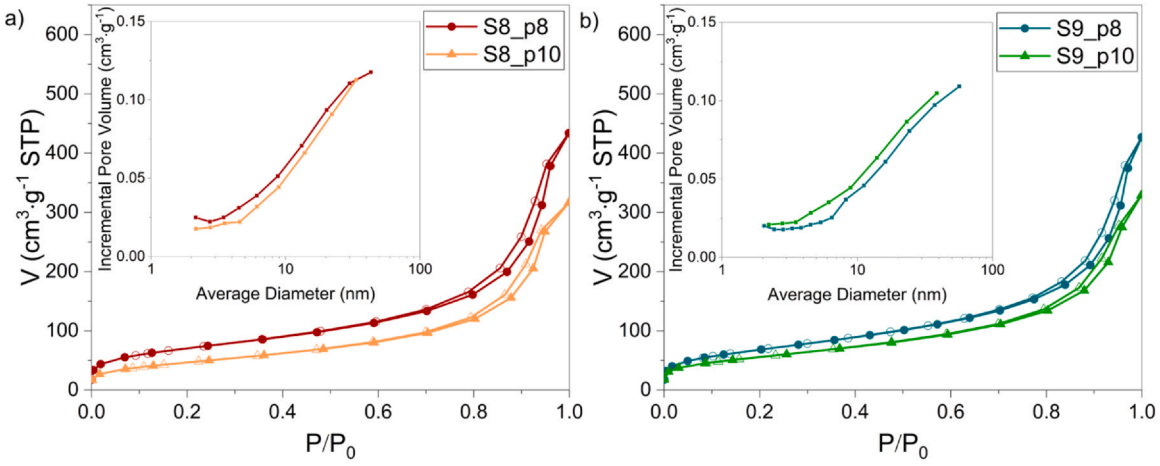

Fig. 2. N_2 physisorption isotherms of ceramic aerogels: a) S8 series; b) S9 series.

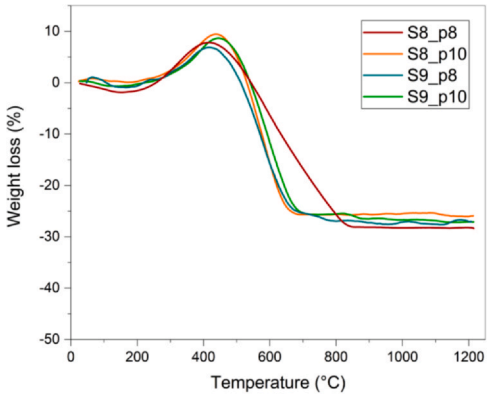

Fig. 3. Oxidative TGA curves of the ceramic aerogels.

Table 3
Mass fraction of monohydrated salt in the composite specimens after vacuum impregnation and dehydration. Residual volumes of pores after deposition and hydration are given too.

Label	Mass fraction of $MgSO_4.1H_2O$ (%)	Residual Volume of pores (%) -$MgSO_4.1H_2O$	Residual Volume of pores (%) -$MgSO_4.7H_2O$
iS8_p8	43.6	61.4	0.1
iS8_p10	36.7	69.6	21.2
iS9_p8	59.1	72.5	28.7
iS9_p10	57.7	74.4	33.7

3.2. Characterization of stabilized $MgSO_4$

All aerogels were weighed before and after impregnation to define their efficiency in retaining the magnesium sulphate salt. The salt uptake was measured after dehydrating all specimens to the monohydrated form at 220 °C for 24 h [11]. Results of salt uptake are summarized in Table 3. As can be deduced, S9 samples are able to retain a higher fraction of salt thanks to the larger fraction of open volume with respect to S8 ones. Considering the theoretical density of $MgSO_4.1H_2O$ and $MgSO_4.7H_2O$, equal to 2.44 g·cm^{-3} and 1.68 g·cm^{-3}, respectively, it is possible to estimate the residual volume of pores after depositing the salt and hydrating it. Table 3 shows that even though the mass fraction of salt is around a half of the total mass of the specimens, the available pore volume is able to accommodate the expansion of the salt upon hydration.

X-ray diffraction and infrared spectra were collected to observe any possible corrosion phenomena or chemical interaction between ceramic support and salt hydrate. FTIR spectra are given in Fig. 4**a**. Neat aerogels present the typical absorption band of asymmetric Si-O-Si stretching at 1000–1100 cm^{-1}, while at 770–800 cm^{-1} a secondary peak arises from the contribution of Si-C bond deformation and Si-O bond stretching [31,32]. Impregnated aerogels, on the other hand, are characterized by a spectrum that resembles the one of pure salt hydrate. As a matter of fact, the contribution of the ceramic skeleton to infrared absorption is less pronounced, if visible. The peaks at 983 cm^{-1}, 1066 cm^{-1}, and 1144 cm^{-1} are all assigned to different stretching vibrations of SO_4^{2-} [33]. Structural water of the salt hydrate can be spotted through the -OH bending vibration at 1630 cm^{-1} and -OH stretching in the broad band spanning from 3000 cm^{-1} to 3500 cm^{-1}. Results of FTIR measurements show that all the spectra of stabilized salt hydrate are built as the superposition of that of $MgSO_4$ and of the relative aerogel. Thus, we can state that there are no specific interactions at the contact interface between the two components.

Similar results can be drawn from the XRD patterns of Fig. 4**b**. In fact, while XRD spectra of neat aerogels are completely amorphous, those of stabilized $MgSO_4$ are in line with that of neat $MgSO_4.7H_2O$, except for the fact that all specimens present peaks of the hexahydrate form ($MgSO_4.6H_2O$, PDF no. 24–0719) as well as those of $MgSO_4.7H_2O$ (PDF no. 36–0419) (the ratio between the two salts varies in the different samples mostly because the hydration state of the salt is extremely sensitive to the lab humidity and temperature).

The impregnation process was characterized by SEM and N_2 physisorption, too. Fig. 5**a** gives an insight into the microstructure of composite specimens, showing deposited salt hydrate on a fracture surface of iS8_p8. As expected, after impregnation and drying some porosity is left unfilled to guarantee a pathway for water vapor during successive hydration cycles. Fig. 5**b** confirms that a certain fraction of pores are left open. Results of BJH adsorption reveal that almost half of the available free pore volume can serve as a hydration path. As a matter of fact, the BJH volume of pores available in iS8_p8 is 0.33 cm^{3}g^{-1}, while before impregnation the pore volume of S8_p8 reaches 0.67 cm^{3}g^{-1}. Remarkably, a fraction of pores smaller than 10 nm are still open and available for vapor transport. Results of other composites are similar to the presented ones.

Raman spectra were acquired on S8 specimens to verify the formation of a free carbon phase within the SiOC matrix during pyrolysis. In Fig. 6, G and D peaks, relative to graphitic carbon and its degree of disorder, are visible at 1585 cm^{-1} and 1305 cm^{-1},

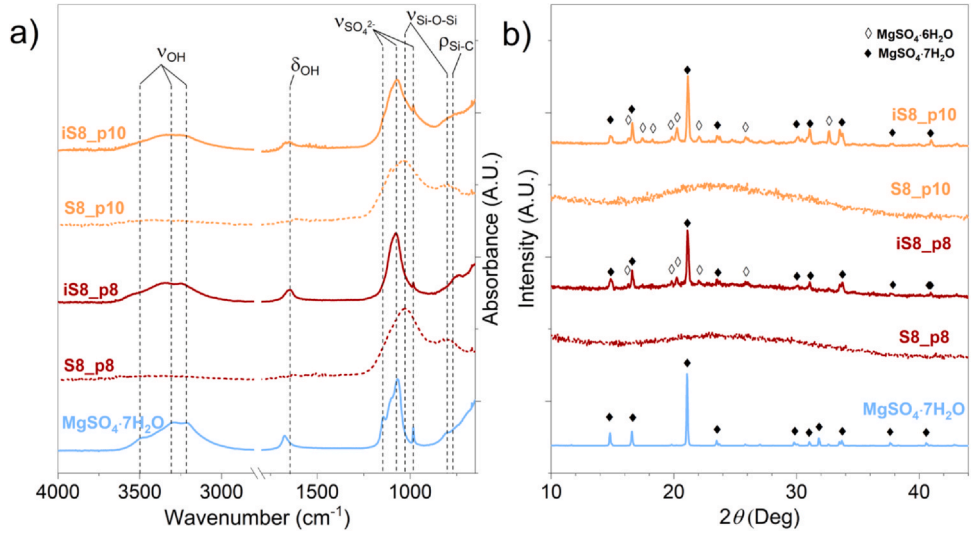

Fig. 4. Representative ATR and XRD spectra of neat and impregnated aerogels of S8 and S9 series: a) ATR spectra; b) XRD spectra.

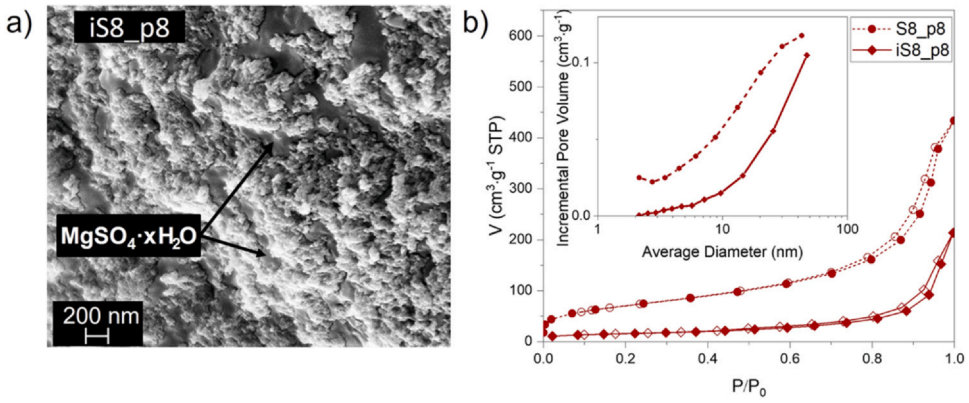

Fig. 5. a) FE-SEM micrograph of iS8_p8 showing the deposition of $MgSO_4 \cdot xH_2O$ inside the porous network of the aerogel; b) N_2 physisorption results of specimen S8_p8 before and after impregnation.

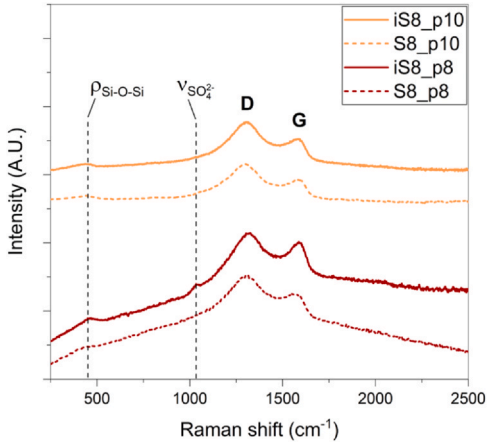

Fig. 6. Raman spectra of S8_p8 and S8_p10 before and after impregnation.

Table 4
Hydration time of the prepared specimens over 5 cycles.

Cycle no.	Temp. (°C)	iS8_p8	iS8_p10	iS9_p8	iS9_p10
		Hydration time (h)			
I	25.5	13.2	3.4	13.2	10.6
II	24.5	14.7	4.2	16.1	12.8
III	24.0	15.7	4.6	17.7	14.1
IV	21.1	17.4	4.9	18.8	14.8
V	24.2	14.3	5.9	15.9	12.8

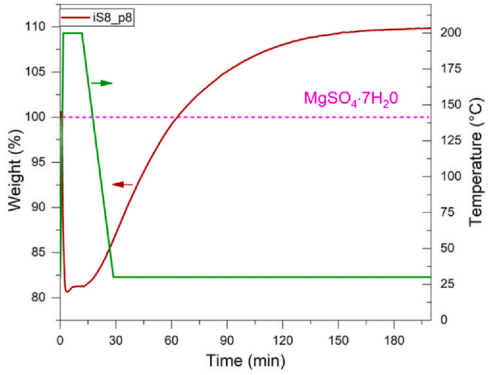

Fig. 8. Dehydration-hydration curve of iS8_p8 under humid air flow.

respectively. Thus, the structures of amorphous aerogels are characterized by an ordered carbon phase in the SiOC matrix, with a certain degree of disorder [34,35].

The weak and broad signal at 450 cm^{-1} is relative to the rocking mode of Si-O-Si bonds belonging to the amorphous SiOC network [36]. Finally, the Raman spectrum of iS8_p8 shows a weak peak at 1040 cm^{-1} that can be assigned to the stretching of SO_4^{2-} tetrahedra [37].

The reliability of the novel composites over hydration/dehydration cycles was then measured by placing them inside a laboratory glass bell with water on its bottom. Hydration to the heptahydrate form was considered concluded as the theoretical weight gain (i.e.

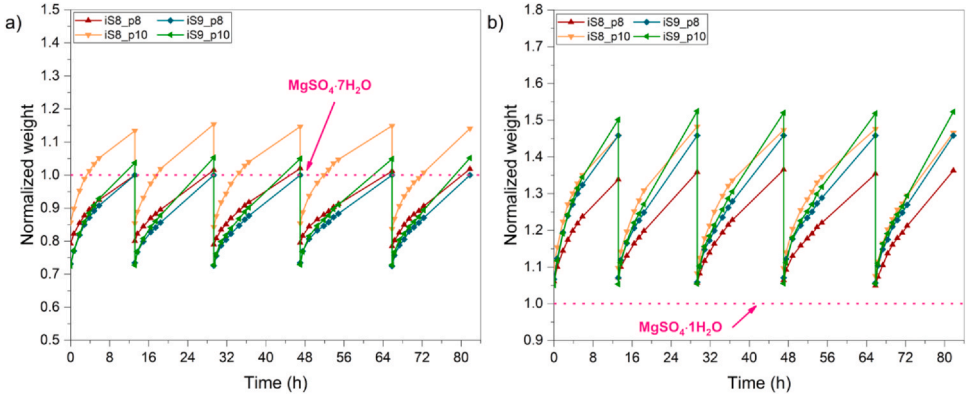

Fig. 7. Water moles uptake test in standard conditions: a) Composite specimens weight uptake normalized over the heptahydrate form; b) composite specimens weight uptake normalized over the monohydrate form.

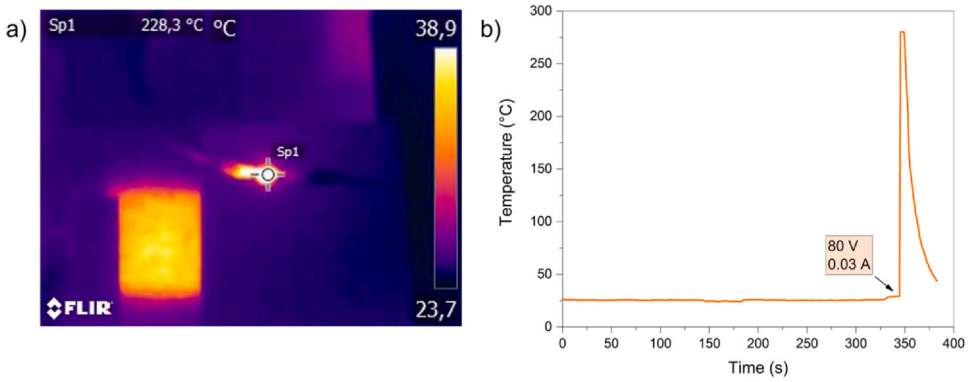

Fig. 9. Thermocamera measurement on the Joule effect of sample S8p10: a) recorded temperature as 80 V are applied on the specimen (positioned in Sp1); b) thermal behaviour as a function of time.

77.57% from monohydrated to heptahydrated $MgSO_4$) of the salt fraction within the aerogels was reached. Five consecutive cycles were recorded and reported in Fig. 7**a,b**. Note that the weight gain can surpass the theoretical one because the salt is hygroscopic and could absorb extra water on its surface. A typical hydration requires between 2 and 14 h to reach the heptahydrate form of magnesium sulphate when specimens are kept in the described conditions. No sulfate crust formed on the surface of the analyzed specimens and the time required for the completion of the hydration cycle remains substantially constant (although a certain scattering of the results can be related to small variations of the lab temperature, Table 4). Clearly, the time required by the various specimens to hydratate is strictly related to the fraction of stored salt. For instance, in every cycle it takes no more than 6 h for sample iS8_p10 to completely reach the heptahydrate form, while samples containing higher fractions of salt (see for example iS9_p8) require at least 10 h.

Hydration can be boosted using water vapor instead of static humid air. A single test on iS8_p8 shows that with RH~100% in flowing air, which is a typical setup of many of the STES prototypes found in literatures [3,38], can induce a complete hydration in about 60 min. The hydration curve is given in Fig. 8.

Remarkably, SiOC aerogels of this kind are electrically semiconductive, meaning that Joule effect can be exploited to induce a fast dehydration of $MgSO_4$ if needed. As a proof, a nearly rectangular specimen of S8p10 was subjected to a controlled voltage while recording its temperature with a thermocamera. Its surface temperature as a function of time is given in Fig. 9. Considering the geometry of the specimen, a resistivity of 6.67 Ω·m can be tentatively calculated. Even though the electrical to thermal conversion is not an efficient process and results in the loss of a "pure" form of energy, such characteristic of these aerogels could be employed when critical conditions (i.e. absence of water vapour) require a fast heating of these STES elements, or when excess electrical energy has to be stored for long periods of time, restoring the thermochemical energy of hydrated magnesium sulphate through direct heating.

3.3. Future research

The thermochemical performances of STES composites strictly depend on the device utilized for their calculation. Thus, to define in an appropriate way the benefits coming from the stabilization of the $MgSO_4$ salt with SiOC aerogels, future researches should focus on the use of a STES reactor for such purpose, relating the confinement effect to the cyclability of these composites with respect to the use of neat salt. Besides, measurements of thermal conductivity of these SiOC aerogels might help for an optimization of the synthesis recipe, tuning porosity, free carbon content and eventually the salt uptake to boost the thermal performances of the composite.

4. Conclusions

In this work the use of a SiOC aerogel as host material for STES applications is presented for the first time. The main results are summarized in the following points:

- SPR-036-based aerogels with tunable piorosity (up to 80%) and SSA comprised between 170 $m^2\ g^{-1}$ and 250 $m^2\ g^{-1}$ were successfully synthesized. After vacuum impregnation in a saturated $MgSO_4$ solution, the maximum $MgSO_4$ uptake of anhydrous salt is 59.1%.
- FTIR, XRD and Raman show that $MgSO_4$ salt does not react with the SiOC aerogel.
- Hydration/dehydration performances of stabilized $MgSO_4$ are characterized by good cyclability and fast hydration rates within 50 min.
- These novel SiOC aerogels show a fairly good electrical conductivity which can be exploited for electrical-to-thermochemical energy conversion and storage through Joule heating of the $MgSO_4$ salt.

The obtained results confirmed that ceramic aerogels represent a new versatile host material in the growing field of thermal energy storage, opening to new perspectives on the employment of polymer-derived ceramics.

Funding

This work was supported by the Italian Ministry of Education, University and Research (MIUR) within the program, PRIN2017 - 2017PMR932 "Nanostructured Porous Ceramics for Environmental and Energy Applications".

CRediT authorship contribution statement

Andrea Zambotti: Conceptualization, Investigation, Data curation, Writing – original draft. **Francesco Valentini:** Investigation, Conceptualization. **Emanuele Lodi:** Investigation, Data curation. **Alessandro Pegoretti:** Resources, Conceptualization. **Václav Tyrpekl:** Investigation. **Soňa Kohúteková:** Investigation. **Matouš Kloda:** Investigation. **Gian D. Sorarù:** Resources, Supervision, Conceptualization, Writing – review & editing, Funding acquisition. **Mattia Biesuz:** Conceptualization, Supervision, Writing – review & editing.

Declaration of Competing Interest

The authors declare that they have no known competing financial interests or personal relationships that could have appeared to influence the work reported in this paper.

References

[1] The EU Emission Trading System in 2020: trends and projections, European Environment Agency, 2020, pp. 1–8.
[2] EEA, Trends and projections in Europe 2013, 2013. eea.europa.eu.
[3] V. Palomba, A. Frazzica, Recent advancements in sorption technology for solar thermal energy storage applications, Sol. Energy 192 (2019) 69–105, https://doi.org/10.1016/j.solener.2018.06.102
[4] A.J. Carrillo, J. González-Aguilar, M. Romero, J.M. Coronado, Solar energy on demand: a review on high temperature thermochemical heat storage systems and materials, Chem. Rev. 119 (2019) 4777–4816, https://doi.org/10.1021/acs.chemrev.8b00315
[5] Q. Li, X. Ma, X. Zhang, J. Zhang, J. Ma, X. Hu, Y. Lan, Preparation of a new capsule phase change material for high temperature thermal energy storage, J. Alloy. Compd. 868 (2021) 159179, https://doi.org/10.1016/j.jallcom.2021.159179
[6] B. Bogdanovic, A. Reiser, K. Schlichte, B. Spliethoff, B. Tesche, Thermodynamics and dynamics of the Mg—Fe—H system and its potential for thermochemical thermal energy storage, ChemInform 34 (2003) 77–89, https://doi.org/10.1002/chin.200305013
[7] J. Pereira da Cunha, P. Eames, Thermal energy storage for low and medium temperature applications using phase change materials - a review, Appl. Energy 177 (2016) 227–238, https://doi.org/10.1016/j.apenergy.2016.05.097
[8] P.A.J. Donkers, L.C. Sögütoglu, H.P. Huinink, H.R. Fischer, O.C.G. Adan, A review of salt hydrates for seasonal heat storage in domestic applications, Appl. Energy 199 (2017) 45–68, https://doi.org/10.1016/j.apenergy.2017.04.080
[9] F. Kleiner, K. Posern, A. Osburg, Thermal conductivity of selected salt hydrates for thermochemical solar heat storage applications measured by the light flash method, Appl. Therm. Eng. 113 (2017) 1189–1193, https://doi.org/10.1016/j.applthermaleng.2016.11.125
[10] L. Tabard, E. Prud'Homme, V. Garnier, L. Gremillard, Hierarchical salt-ceramic composites for efficient thermochemical energy storage, Appl. Mater. Today 20 (2020), https://doi.org/10.1016/j.apmt.2020.100658
[11] S. Hongois, F. Kuznik, P. Stevens, J.J. Roux, Development and characterisation of a new MgSO4-zeolite composite for long-term thermal energy storage, Sol. Energy Mater. Sol. Cells 95 (2011) 1831–1837, https://doi.org/10.1016/j.solmat.2011.01.050
[12] C. Xu, Z. Yu, Y. Xie, Y. Ren, F. Ye, X. Ju, Study of the hydration behavior of zeolite-MgSO4 composites for long-term heat storage, Appl. Therm. Eng. 129 (2018) 250–259, https://doi.org/10.1016/j.applthermaleng.2017.10.031
[13] A. Hauer, Evaluation of adsorbent materials for heat pump and thermal energy storage applications in open systems, Adsorption 13 (2007) 399–405, https://doi.org/10.1007/s10450-007-9054-0
[14] S.Z. Xu, R.Z. Wang, L.W. Wang, J. Zhu, Performance characterizations and thermodynamic analysis of magnesium sulfate-impregnated zeolite 13X and activated alumina composite sorbents for thermal energy storage, Energy 167 (2019) 889–901, https://doi.org/10.1016/j.energy.2018.10.200
[15] D. Mahon, G. Claudio, P.C. Eames, An experimental investigation to assess the potential of using MgSO4 impregnation and Mg2+ ion exchange to enhance the performance of 13X molecular sieves for interseasonal domestic thermochemical energy storage, Energy Convers. Manag 150 (2017) 870–877, https://doi.org/10.1016/j.enconman.2017.03.080
[16] K. Posern, C. Kaps, Calorimetric studies of thermochemical heat storage materials based on mixtures of MgSO4 and MgCl2, Thermochim. Acta 502 (2010) 73–76, https://doi.org/10.1016/j.tca.2010.02.009
[17] S.P. Casey, D. Aydin, S. Riffat, J. Elvins, Salt impregnated desiccant matrices for "open" thermochemical energy storage - Hygrothermal cyclic behaviour and energetic analysis by physical experimentation, Energy Build. 92 (2015) 128–139, https://doi.org/10.1016/j.enbuild.2015.01.048
[18] K. Posern, K. Linnow, M. Niermann, C. Kaps, M. Steiger, Thermochemical investigation of the water uptake behavior of MgSO4 hydrates in host materials with different pore size, Thermochim. Acta 611 (2015) 1–9, https://doi.org/10.1016/j.tca.2015.04.031
[19] H.A. Ousaleh, S. Said, A. Zaki, A. Faik, A. El Bouari, Silica gel/inorganic salts composites for thermochemical heat storage: improvement of energy storage density and assessment of cycling stability, Mater. Today Proc. 30 (2019) 937–941, https://doi.org/10.1016/j.matpr.2020.04.354
[20] S.C. Akcaoglu, Z. Sun, S.C. Moratti, G. Martinopoulos, Investigation of novel composite materials for thermochemical heat storage systems, Energies 13 (2020) 1042, https://doi.org/10.3390/en13051042
[21] L. Calabrese, V. Brancato, V. Palomba, A. Frazzica, L.F. Cabeza, Magnesium sulphate-silicone foam composites for thermochemical energy storage: assessment of dehydration behaviour and mechanical stability, Sol. Energy Mater. Sol. Cells 200 (2019) 109992, https://doi.org/10.1016/j.solmat.2019.109992
[22] H. Ait Ousaleh, S. Sair, A. Zaki, A. Younes, A. Faik, A. El Bouari, Advanced experimental investigation of double hydrated salts and their composite for improved cycling stability and metal compatibility for long-term heat storage technologies, Renew. Energy 162 (2020) 447–457, https://doi.org/10.1016/j.renene.2020.08.085
[23] A. Vasu, F.Y. Hagos, M.M. Noor, R. Mamat, W.H. Azmi, A.A. Abdullah, T.K. Ibrahim, Corrosion effect of phase change materials in solar thermal energy storage application, Renew. Sustain. Energy Rev. 76 (2017) 19–33, https://doi.org/10.1016/j.rser.2017.03.018
[24] M.C. Browne, E. Boyd, S.J. McCormack, Investigation of the corrosive properties of phase change materials in contact with metals and plastic, Renew. Energy 108 (2017) 555–568, https://doi.org/10.1016/j.renene.2017.02.082
[25] P. Colombo, G. Mera, R. Riedel, G.D. Sorarù, Polymer-derived ceramics: 40 years of research and innovation in advanced ceramics, J. Am. Ceram. Soc. 93 (2010) 1805–1837, https://doi.org/10.1111/j.1551-2916.2010.03876.x
[26] G.D. Sorarù, C. Tavonatti, L. Kundanati, N. Pugno, M. Biesuz, Effect of the pyrolysis atmosphere on the mechanical properties of polymer-derived SiOC and SiCN, J. Am. Ceram. Soc. 103 (2020) 6519–6530, https://doi.org/10.1111/jace.17392
[27] P. Vallachira Warriam Sasikumar, E. Zera, M. Graczyk-Zajac, R. Riedel, G.D. Soraru, B. Dunn, Structural design of polymer-derived SiOC ceramic aerogels for high-rate Li ion storage applications, J. Am. Ceram. Soc. 99 (2016) 2977–2983, https://doi.org/10.1111/jace.14323
[28] S. Aguirre-Medel, P. Jana, P. Kroll, G.D. Sorarù, Towards porous silicon oxycarbide materials: effects of solvents on microstructural features of poly(methylhydrosiloxane)/divynilbenzene aerogels, Materials (Basel) 11 (2018), https://doi.org/10.3390/ma11122589
[29] G.D. Sorarù, E. Zera, R. Campostrini, Aerogels from preceramic polymers, in: Handb, Sol. Gel Sci. Technol. (2017), https://doi.org/10.1007/978-3-319-19454-7_121-1
[30] I. Union, O.F. Pure, A. Chemistry, Reporting physisorption data for gas / solid systems with special reference to the determination of surface area and porosity, Area 57 (1985) 603–619, https://doi.org/10.1351/pac198557040603
[31] R. Al-Oweini, H. El-Rassy, Synthesis and characterization by FTIR spectroscopy of silica aerogels prepared using several Si(OR)4 and R′′Si(OR′)3 precursors, J. Mol. Struct. 919 (2009) 140–145, https://doi.org/10.1016/j.molstruc.2008.08.025
[32] V.L. Nguyen, N.B. Laidani, G.D. Sorarù, N-doped polymer-derived Si(N)OC: the role of the N-containing precursor, J. Mater. Res. 30 (2015) 770–781, https://doi.org/10.1557/jmr.2015.44
[33] F. Ovalles, M. Gallignani, R. Rondón, M.R. Brunetto, R. Luna, Determination of sulphate for measuring magnesium sulphate in pharmaceuticals by flow analysis-fourier transforms infrared spectroscopy, Lat. Am. J. Pharm. 28 (2009) 173–182.
[34] W. Duan, X. Yin, F. Ye, Q. Li, M. Han, X. Liu, Y. Cai, Synthesis and EMW absorbing properties of nano SiC modified PDC-SiOC, J. Mater. Chem. C 4 (2016) 5962–5969, https://doi.org/10.1039/c6tc01142j
[35] A.C. Ferrari, J. Robertson, Interpretation of Raman spectra of disordered and amorphous carbon, Phys. Rev. B 61 (2000) 14095–14107, https://doi.org/10.1103/PhysRevB.61.14095
[36] R.K. Biswas, P. Khan, S. Mukherjee, A.K. Mukhopadhyay, J. Ghosh, K. Muraleedharan, Study of short range structure of amorphous Silica from PDF using Ag radiation in laboratory XRD system, RAMAN and NEXAFS, J. Non Cryst. Solids 488 (2018) 1–9, https://doi.org/10.1016/j.jnoncrysol.2018.02.037
[37] A. Wang, J.J. Freeman, B.L. Jolliff, I.M. Chou, Sulfates on mars: a systematic raman spectroscopic study of hydration states of magnesium sulfates, Geochim. Cosmochim. Acta 70 (2006) 6118–6135, https://doi.org/10.1016/j.gca.2006.05.022
[38] M. Schmidt, M. Linder, Power generation based on the Ca(OH)2/ CaO thermochemical storage system – experimental investigation of discharge operation modes in lab scale and corresponding conceptual process design, Appl. Energy 203 (2017) 594–607, https://doi.org/10.1016/j.apenergy.2017.06.063